

Chapter 6:

Probing bias and power dependency of high performance broadband Mg/ZnSnP₂/Sn back-to-back Schottky junction photodetectors

6.1. Introduction

The fabrication of broadband photodetectors (PDs) with the capability of detecting optical photons over the spectral range from UV to NIR using low-cost and high-efficient new material is very important and relevant for their wide-scale use in various applications such as telecommunication, conventional imaging, medical diagnostics, neuroscience research, environmental observation, machine vision, robotics, motion detection, day-night surveillance etc. [1–6]. Recently, the 2D layered materials like graphene, black phosphorus (BP), MoS₂-WS₂, Bi₂O₂Se, etc. have opened up new prospects in the field of photodetectors [7–12]. The zero bandgaps, relatively low absorption coefficient and a short photo-carrier lifetime of graphene limit its application in the optoelectronic devices [13–15]. Usually, the graphene-based PDs are associated with a low value of responsivity of the order of 10^{-3} AW⁻¹ [16]. Furthermore, the BP and the transition metal di-chalcogenides need to account for the instability issues along with the complexity of their fabrication processes [17]. Recently, organolead triiodide perovskite-based PD has shown very high responsivity [18]. The constituent elements of this material contain Pb which limits its application on a large scale due to environmental issues. Many attempts have also been made to develop Pb-free perovskite materials for PD application. However, the response and recovery speed of such PDs are not satisfactory [19, 20]. The discovery of new materials with desirable optical properties is still a challenging field of research. A Pb-free direct bandgap ternary semiconducting material ZnSnP₂ has been considered recently which shows promising optical properties in the visible to NIR range of the optical spectrum [21]. In our previous report, we have clearly shown that the responsivity of Mg/ZnSnP₂/Sn PD is 27 mA W⁻¹ with a very fast rise time of 47 μ s [22]. Although the time of rise of the device was very fast, the value of the responsivity was not so satisfactory considering the performance of similar PD based devices. It was found that the two SJs eventually determine the overall performance of the PDs. Thus, in this work two SJs are considered independently to thoroughly investigate the involved basic processes in the same device configuration on the performance of the fabricated devices.

It is worth noting that the working of a PD essentially depends on different types of defects due to impurities and lattice mismatching with the substrate. Usually, the presence of defects deteriorates device performance by preventing the photogenerated carriers to reach the electrical contacts. However, a recent work by Dong et al. [23] shows that such defect mediated states could also be useful for significantly enhancing the value of responsivity, detectivity, bandwidth and operational speed of the PD fabricated using perovskite CH₃NH₃PbI₃ with and

without C_{60} surface passivation layer. The performance of the PD without C_{60} layer was much superior due to the creation of hole trapping centers by the defects. Therefore, a detailed investigation of the capture mechanism of photogenerated carriers by the defect states and their re-emission from the captured state with the applied biases and illumination intensities of the fabricated devices are undertaken in this current research program. In our view, this investigation will create interest to study the basic mechanism involved in BTB PDs not only using $ZnSnP_2$ but also other materials for future device applications.

In the current work, we have studied the photodetection properties of two Schottky junction (SJ) diodes viz., $Mg/ZnSnP_2$ and $Sn/ZnSnP_2$ connected BTB in series on a coplanar surface, under different illumination power at a fixed wavelength of 650 nm. The current-voltage (I–V) characteristics of the two junctions were measured in the dark and also illuminating them independently. The variation of photocurrent (I_{ph}), responsivity (R), detectivity (D) and gain (G), response and recovery speed of the fabricated SJs were estimated under the variable illumination power and applied reverse bias ranging from 0 to 2.5 V. Frequency and illumination dependent capacitance measurements were carried out to estimate the variation of occupancy of the defect states due to photon absorption. A plausible mechanism associated with trapping and de-trapping of photogenerated carriers was also incorporated to explain the obtained unusual behaviors of the devices.

6.2. Experimental

6.2.1. Material synthesis

The synthesis of the bulk material $ZnSnP_2$ for the deposition of thin films was done by the solvent technique [24] owing to the high vapor pressure of phosphorus. To obtain $ZnSnP_2$ ingot, the constituent elements were sealed in an ampoule with excess Sn concentration, which acts as a solvent ($ZnSnP_2$: Sn=1:3). Before sealing, it was evacuated to a vacuum of 10^{-3} mbar. All the other controlling growth parameters are already mentioned in detail in section 4.2 of chapter four. The as-synthesized ingot was further treated with 0.1 M HCl to extract pure $ZnSnP_2$ in powder form. This powder was then used as the source material to deposit the thin film on p-type silicon (Si) (100) and glass substrates by thermal evaporation. Prior to the deposition Si substrate was successively treated with 40% pure hydrofluoric acid and acetone while for the glass we have used chromic acid. A paste was formed by adding alcohol to the $ZnSnP_2$ powder which was then placed in a boat-shaped tungsten filament for evaporation. The thin film growth was performed at substrate temperature and pressure of 300 °C and 10^{-6} mbar,

respectively. The film deposition rate (1 nm/s) and the film thickness ($\sim 0.3 \mu\text{m}$) were monitored by a quartz crystal monitor attached with the deposition system. After deposition, the films were annealed at 300°C for 1 hour in the vacuum of $\sim 10^{-6}$ mbar.

6.2.2. Device fabrication

In order to achieve two asymmetric Schottky diodes connected in BTB configuration, Sn and Mg contacts were deposited on the thin film also using the TE technique. We have used a mica sheet as a mask, to deposit the metal contacts with desirable shape and size. After the deposition, only the Sn contact was annealed at a temperature of 300°C for a period of 1 hour at an air pressure of $\sim 10^{-6}$ mbar. Both the contacts were dimensionally identical having an area of 0.0314 cm^2 . The ZnSnP_2 thin film was chemically treated before loading into the deposition chamber to remove any unintentionally formed oxide layer on the surface and other chemical impurities. We have used silver paste (manufactured by Sigma Aldrich) and copper wire for connecting the device with the measuring instruments. The entire growth process is illustrated in Figure 6.1.

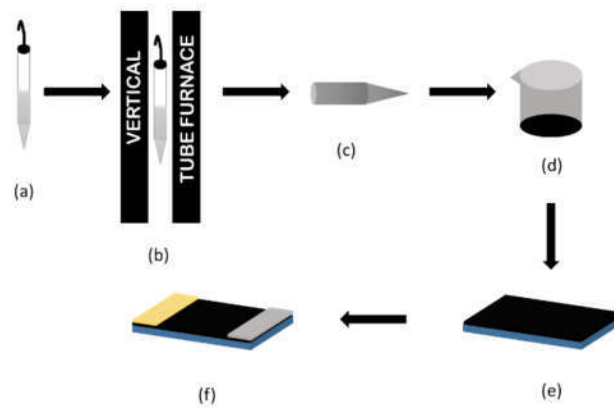


Figure 6.1. Schematic representation of the growth process. (a) ampoule containing Zn, Sn and P was sealed (b) Placed in a vertical tube furnace and heated 700°C for 24 hours (c) obtained ingot (d) Ingot was treated with 0.1 M HCl to remove Sn (e) Thin-film was deposited by thermal evaporation (f) Metal contacts were deposited by thermal evaporation.

6.2.3. Characterization

6.2.3.1. Structural and optical characterization of the thin film

Grazing incidence x-ray diffraction (GIXRD) technique at CuK_α line (Rigaku Smart Lab) was employed to extract the information about the crystallinity and microstructure of the film. The generator was powered by applying 40 kV potential difference and 40 mA current. The

bandgap of the films was estimated by recording the absorbance (A) spectra at room temperature using Perkin Elmer Lambda-750 spectrophotometer.

6.2.3.2. Device characterization

6.2.3.2.1. Photocurrent measurement

We have used Keithley 4200 SCS and Tektronix TBS2102 oscilloscope to measure I–V characteristics and temporal response at a fixed bias, respectively at room temperature with different illumination intensity. A diode laser of wavelength 650 nm was used as a source to illuminate only the Schottky junctions (SJs) and their periphery.

6.2.3.2.2. Temporal measurement

A schematic representation of the experimental setup for the study of the temporal variation is depicted in Figure. 6.2. The signal was measured across a resistance connected in series with the device using an oscilloscope when devices were operated under the biased condition. However, the oscilloscope was connected directly across the devices self-powered mode of operation. To produce a square-shape optical pulse, the laser was driven by an ultrafast function generator to avoid the convolution effect. During the measurement, the frequency of the function generator was kept fixed at 70 Hz. However, we have also carried out the temporal measurement with the variation of frequency of the source and illuminating the sample with different frequency of light. For the later one three different diode lasers having frequency 325 nm, 450 nm and 780 nm were used. In ordered to find the contribution of the intensity of the light over response and recovery speed of the PDs, a variable neutral density filter was placed such a way that light goes through it before illuminating the sample.

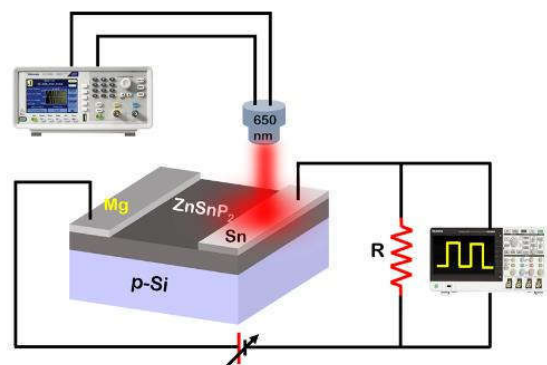


Figure 6.2. Representation of the temporal measurement setup with Schematic representation of the Mg/ZnSnP₂/Sn photodetector.

6.2.3.2.3. Frequency and illumination intensity dependent capacitance measurement

Frequency dependent capacitance (c-f) and illumination intensity dependent photo-capacitance measurements have been carried out using Keithly 4200 SCS in conjunction with the matrix unit. A diode laser of wavelength 650 nm was used to illuminate the both the junction independently for photocapacitance measurements. Extra care was taken to keep the other junction under dark. For the intensity variation measurement, a variable neutral density filter was placed between the laser and the sample.

6.3. Result and discussions

The crystallinity and the value of the bandgap of the as-deposited ZnSnP_2 thin film were determined by employing GIXRD and optical absorption spectroscopic techniques, respectively. The performance parameters (responsivity, detectivity, gain, and speed) of the fabricated PDs were also investigated from the I-V data recorded under different conditions.

6.3.1. GIXRD measurement

Initially, the as-deposited film on p-type Si (100) substrate was considered for GIXRD measurement at room temperature showing multiple diffraction related peaks (Figure 6.3). The peaks are correlated to (112), (200), (004), (303) and (316) planes of ZnSnP_2 were identified by comparing the data with the available JCPDS file [No: 73-0396] for this material. Multiple peaks in the GIXRD data confirm the polycrystalline nature of the film. Significant width of the diffraction peaks is the consequence of the small crystallite size which was calculated to be of ~ 7 nm implementing the Scherrer formula (equation 5.11).

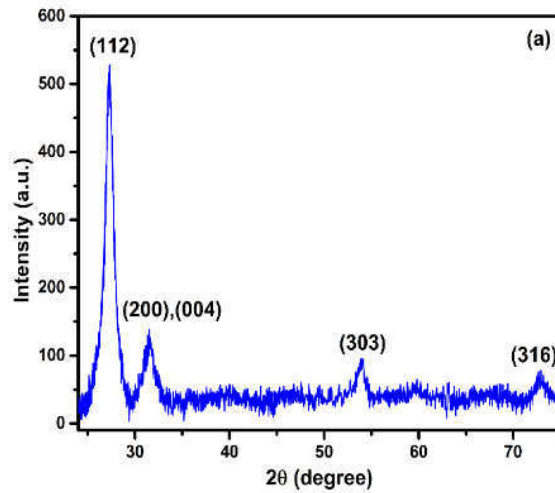


Figure 6.3. Grazing incidence x-ray diffraction of ZnSnP_2 on Si.

6.3.2. Optical absorption spectroscopy

The variation in the value of α with the incident wavelength is illustrated in Figure 6.4 (a). The as-grown film showed a threshold value of α corresponding to the incident wavelength of ~ 850 nm (1.46 eV) implying the deposited film was fairly dominated by chalcopyrite phases of ZnSnP_2 as predicted by VASP based hybrid density functional theory calculation. Figure 6.4(b) shows the optical absorption spectra in the form of $(\alpha h\nu)^2$ vs $h\nu$ plot for the film grown on glass, where α is the absorption coefficient of the films, h is the Planck constant and ν is the frequency of light. The room temperature bandgap of the film was found to be ~ 1.46 eV by extrapolating the linear region of the graph $((\alpha h\nu)^2$ vs $h\nu$) to the $h\nu$ axis.

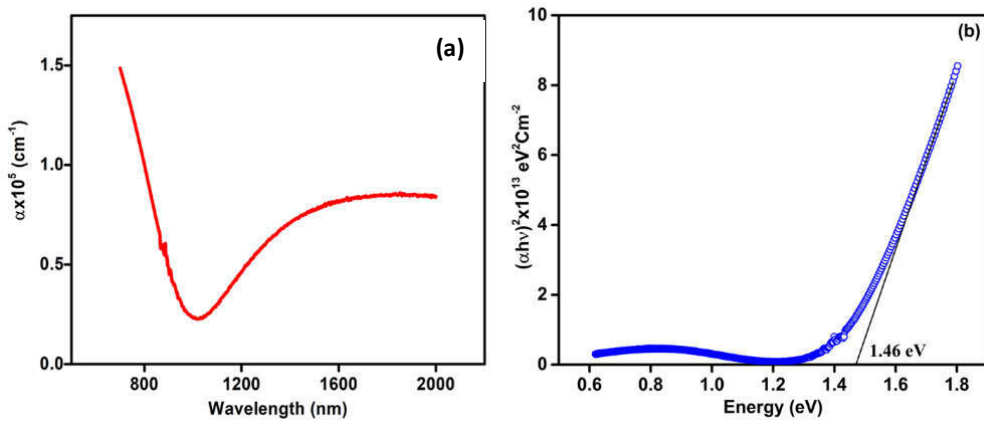


Figure 6.4 (a) The variation of α with wavelength (b) Optical absorbance spectra of ZnSnP_2 grown on the glass substrate.

6.3.3. Current-voltage characteristics

The I–V characteristic curves of the $\text{Mg}/\text{ZnSnP}_2/\text{Sn}$ BTB connected Schottky diodes with and without illumination are depicted in Figures 6.5(a) and (b), respectively. The current increased exponentially in the forward bias regime (Mg to +ve, Sn to -ve), whereas in the reverse bias it showed an almost linear relationship with applied voltage. This asymmetrical nature can be correlated to the formation of a higher barrier height at J_1 (Mg/ZnSnP_2) than J_2 (Sn/ZnSnP_2) due to their different work functions. Usually, devices where two rectifying junctions are connected in BTB configuration show roll-over like behavior [25, 26] in both the biases, as it has been observed for $\text{Mg}/\text{ZnSnP}_2/\text{Sn}$ structure [22]. Beyond the roll-over voltage, current in the MSM structure either saturates or increases linearly with bias, depending on the nature of the available parallel paths. The value of the roll-over voltage decreases with increasing barrier height. This behavior is limited to the SJ which is in reverse bias at that instant [22]. In the

forward bias, the Mg/ZnSnP₂/Sn device did not exhibit such behavior which is an indication of the increasingly Ohmic character of Sn/ZnSnP₂ junction as a result of annealing. At the time

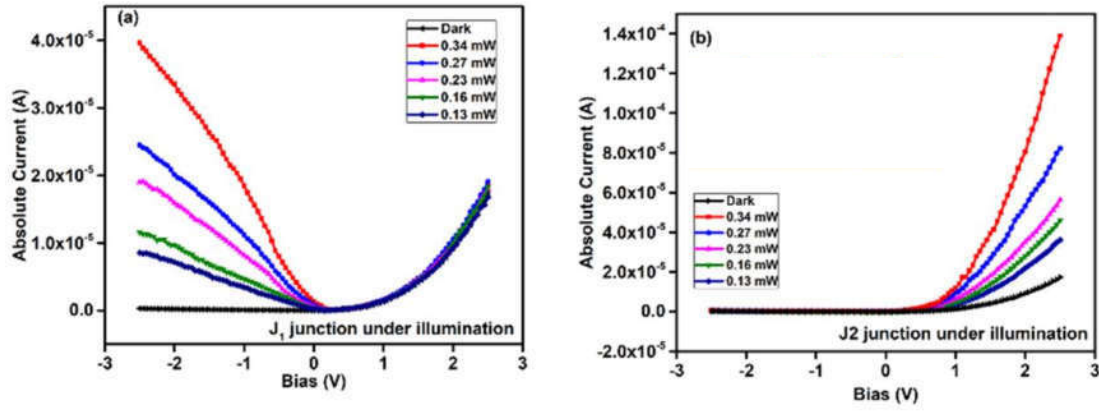


Figure 6.5. (a) I-V curve ranging from -2.5 V to 2.5 V, under dark and light with variable laser power (0.13 mW - 0.34 mW) for the junction J₁. (b) I-V curve ranging from -2.5 V to 2.5 V for J₂ with the illumination of different laser power (mentioned within the graphs) and also in dark.

of voltage sweeping, one of the two SJs was connected to the positive terminal while the other one was connected to the negative terminal of the source meter. The junctions J₁ and J₂ were found in reverse configuration for negative (3rd quadrant of I-V curve) and positive (1st quadrant of I-V curve) bias regions, respectively. When J₁ and J₂ were illuminated indepen-

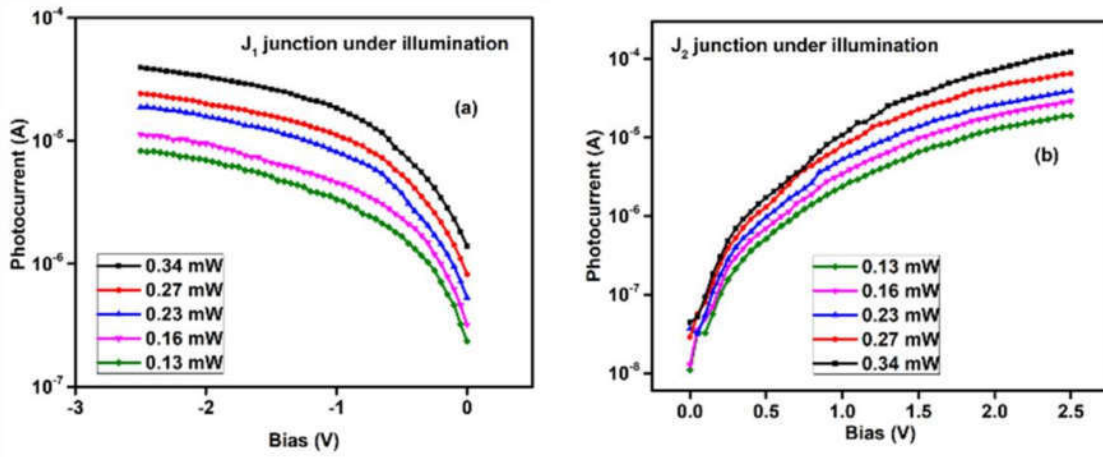


Figure 6.6. Variation of photocurrent during voltage sweep in semi-log scale with different illumination power (0.13 mW to 0.34 mW) for the junctions (a) J₁ (b) J₂.

ntly, only a significant increase in respective reverse and forward bias current were observed (Figure. 6.5) while the current in the opposite configurations remained unchanged. Upon illumination of light, the current showed an increment of almost three orders of magnitude in reverse bias. Figures. 6.6(a) and (b) demonstrate the variation of photocurrents with the applied bias for the variation of illumination power in a semi-log plot which rises with increasing the

forward and reverse bias. The junction J_1 exhibited much better photo response compare to J_2 at 0 V, whereas, this observation changed at high bias. Both the junctions J_1 and J_2 offered the maximum value of photocurrent of 3.77×10^{-5} A and 1.34×10^{-4} A, respectively, when they were operated at 2.5 V reverse bias with respect to each other. The value of the turn-on voltage (V_{TO}) also depends on the power of the incident light which increased with increasing illumination power as shown in Figure. 6.5(a). The splitting of the Fermi levels increased with the increasing power of the illumination which in turn cause a reduction of the barrier height of the junctions. Consequently, the value of V_{TO} has exhibited an increasing trend with increasing power.

6.3.4. Photodetectors performance

6.3.4.1. Bias dependency

In this section, the performance of the PDs was investigated in self-power mode as well as with the application of external bias. A monotonic increment in the value of responsivity, R , was observed in both the conditions of applied bias (Figure. 6.7(a) & (b)). Although for J_1 , the value of R increased almost linearly (Figure. 6.7(a)), the variation became non-linear for J_2 at higher biases (Figure. 6.7(b)). Both the junctions, J_1 and J_2 exhibited responsivity of 0.1 AW^{-1} and 0.03 AW^{-1} at 0 V respectively while at 2.5 V these values reached a maximum of 4.7 AW^{-1}

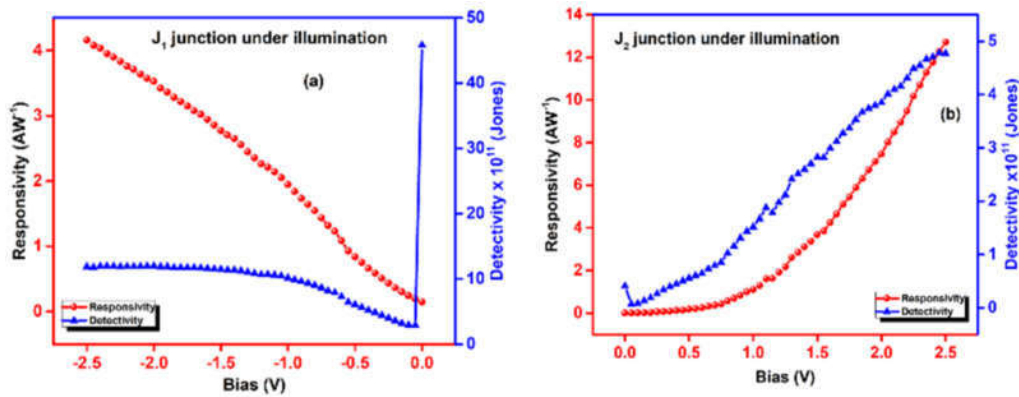


Figure 6.7. Bias dependent responsivity and detectivity for (a) J_1 (b) J_2 . The curves with the red ball and blue triangle represent responsivity and detectivity respectively.

and 12.7 AW^{-1} , respectively, which were almost three orders of magnitude higher than the value for $\text{Mg/ZnSnP}_2/\text{Sn}$ MSM structure reported in the previous chapter. It is noted that the value of R for commercially available Si-based PDs is around 0.1 AW^{-1} [27] which is two orders of magnitude lower than the J_2 junction reported here. The variation of D at J_1 and J_2 is shown with blue traces in Figures. 6.7(a) & (b). For J_1 , the maximum value of D was found to

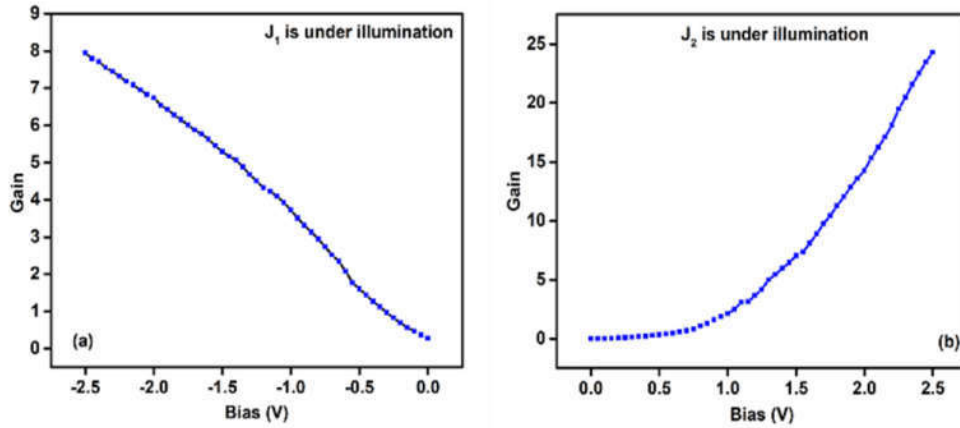


Figure 6.8. The variation of gain with applied bias at fixed illumination wavelength and power (a) J_1 is under illumination (b) J_2 is under illumination.

be 4.62×10^{12} Jones at 0 V followed by a rapid reduction to 2.9×10^{11} Jones at 50 mV. With a further increase in the applied voltage, this value started to increase up to the bias voltage of 1 V. Beyond this voltage, it became almost independent of the applied bias. Such a rapid decrement in the value of D for bias greater than 0 V is owing to the sudden increment of dark current. In the case of J_2 , the value of D showed monotonic increment with an increasing bias voltage which is quite different in comparison to the behavior of J_1 . During the self-powered condition, J_2 delivered a D value of 1.1×10^{11} Jones. At 2.5 V, the obtained values of D s were found to be 1.19×10^{12} Jones and 4.78×10^{11} Jones, respectively, for J_1 and J_2 . It strongly indicates that J_1 and J_2 are very suitable to detect an optical signal of intensity as low as 10^{-12} W and 10^{-11} W, respectively. The maximum detectivity obtained in this study was much higher than the previously reported value for the same structure.

Equation (2.6) in section 2.5.4 suggests that the gain follows a similar nature as that of R which is shown in Figures. 6.8(a) & (b). J_1 and J_2 showed a gain of 7.59 and 24.29 at 2.5 V, respectively. Such a high value of gain is possible when the photogenerated carriers move through several times through the circuit before they recombine which is associated with a very short transit time [28]. Another possible way is the tunneling of photogenerated carriers through the junction owing to the reduced depletion width [29]. Usually, the tunneling of carriers is observed at relatively high bias. Therefore, the contribution of tunneling in the gain mechanism could be neglected in this situation.

The performance of PDs depends on the generation of carriers and their efficient collection into the external circuit. In the structure, where two SJs are connected in BTB configuration, the existing barrier at the other end severely hinders the process of carrier collection in the

external circuit. Under the self-power mode of operation, the photogenerated carriers are separated by the built-in electric field before they recombine, and higher barrier height signifies a stronger built-in electric field. According to the band bending model, the photogenerated electrons do not experience any barrier before being collected at the metal contact, whereas, the photogenerated holes face the barrier at the opposite junction (J_2). Hence, a lower barrier height at J_2 increases hole-collection efficiency. A higher value of R and D , at J_1 without applied field can be correlated to the stronger built-in electric field along with lower barrier height at J_2 . The width of the depletion region at J_1 increases with increasing reverse bias whereas it decreases at the other junction. Beyond flat band condition, no effective barrier for holes exists at the opposite junction (J_2) which significantly enhances the value of R and D . The effect of this condition is more prominent while J_2 remains in reverse bias due to much higher barrier height at J_1 relative to J_2 . So, it is reasonable to correlate the non-linear increase in the value of R with the explanation given above. High photocurrent and low dark current are essentially responsible to achieve a very high value of D at 0 V.

6.3.4.2. Dependency on the intensity of the illumination

The variation of I_{ph} , R and D with different illumination intensity, under self-powered condition, for the junctions J_1 and J_2 are represented in Figures. 6.9 (a), (b), (c) & (d). All these parameters were enhanced with the increasing value of the illumination intensity. Power dependent I_{ph} was fitted using the empirical relation $I_{ph} = CP^\theta$, where C is a constant and P and θ are the power of the illumination and power exponent, respectively. A theoretical model developed by Rose predicts, without any imperfection in the thin film, the value of θ to be unity, although, in presence of traps and recombination centers, it becomes less than one [30, 31]. The defect states present within the forbidden gap of the semiconductor prevent all the photogenerated carriers to reach the electrical contacts which eventually makes the sub-linear increase of photocurrent with the incident illumination power. Both the junctions J_1 and J_2 under the present study exhibited an uncommon super-linear dependence of photocurrent with incident optical power as shown in Figures. 6.9(a) & (b). The obtained values of θ for J_1 and J_2 were 1.75 ± 0.19 and 1.42 ± 0.21 respectively. Recently, PDs based on 2D materials such as Ta_2NiSe_5 and $MoS_2(1-x)Se_{2x}$ exhibit the same super-linear dependence of photocurrent with light power [32, 33].

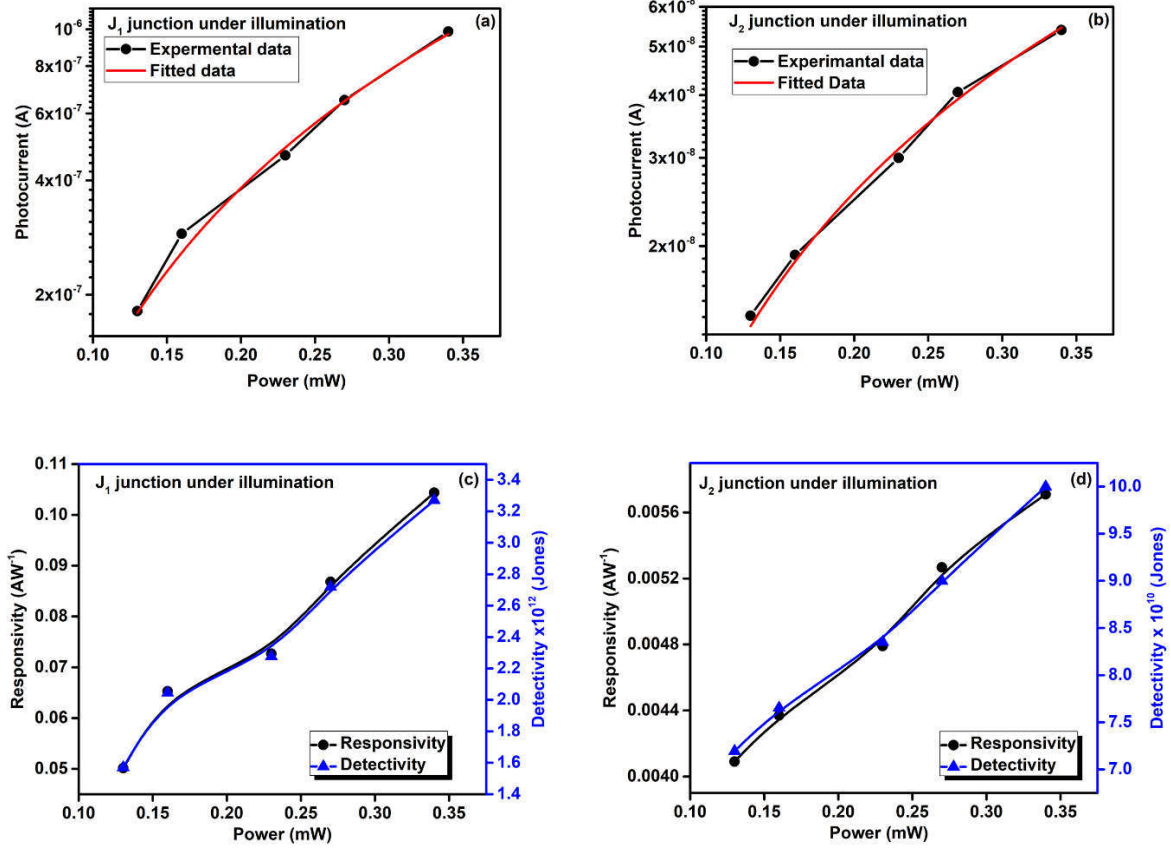


Figure 6.9. Variation of photocurrent with different illumination power at the self-powered configuration in a semi-log scale for (a) J_1 junction (b) J_2 junction. The black line + filled circle represents experimental data and red line is used for the fitted curve using numerical relation $I_{ph} = CP^0$. Variation of responsivity and detectivity of (c) J_1 junction (d) J_2 junction. Black line with square and blue line with triangle represent responsivity and detectivity, respectively.

6.3.4.3. Temporal measurement of the photodetectors

Another essential parameter in PD's performance is the ability to follow a fast time-varying signal which is characterized in terms of rise and decay times. Time responses of J_1 and J_2 under different biasing and illumination powers were also investigated which are shown in Figures. 6.10(a), (b), (c) and (d). PDs were able to detect photons under different bias and illumination power. The sensitivity of the junctions (J_1 and J_2) with variable frequency optical signals were also studied and shown in Figures. 6.11(a), (b), (c), and (d). These measurements were carried out at a fixed bias and illumination power of 0.34 mW. Upon illumination, photocurrent in the junctions (J_1 and J_2) were increased rapidly due to the generation and separation of carriers. The photocurrent decreased sharply after switching off the light. The time required to increase the photocurrent from 10 % to 90 % of its maximum value is defined as the time of rise (τ_r) of the detector while a decrease within these values is called its time of

recovery (τ_d). Obtained values of τ_r and τ_d for J_1 and J_2 were 200 μ s, 2300 μ s, and 390 μ s, 240 μ s, respectively at an operating reverse bias of 2.5 V relative to each other, in presence of 0.34

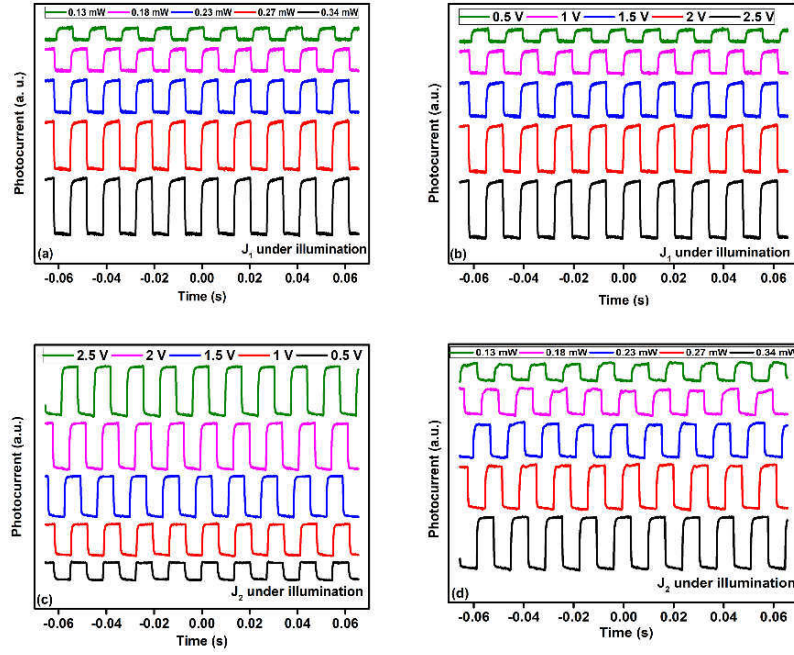


Figure 6.10. Temporal measurements of photodetectors response and recovery time at a fixed frequency of the function generator (a) J_1 is illuminated with different power of illumination (b) J_1 is operated under different applied bias with fixed laser power (c) J_2 is operated under different applied bias with fixed laser power (d) J_2 is illuminated with different power of illumination. The value of the optical powers and biases are mentioned within the graphs.

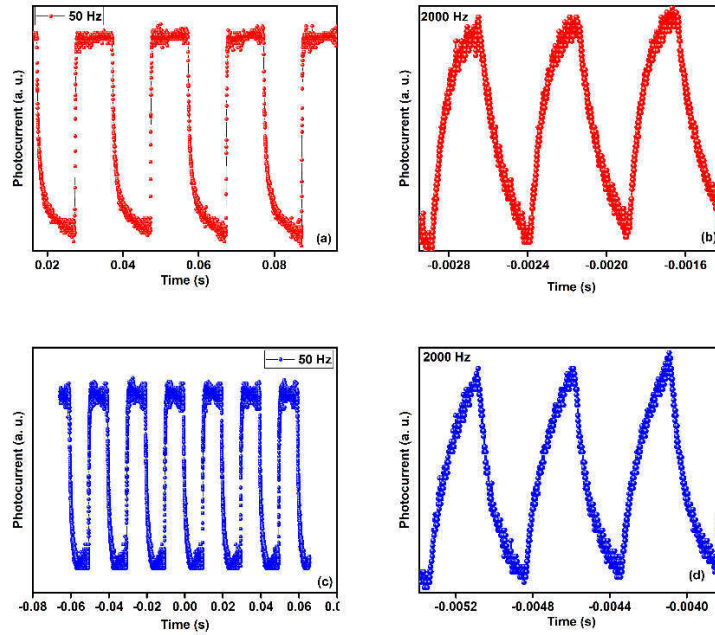


Figure 6.11. Temporal variation of the photodetectors at a fixed bias and illumination with different frequencies (a) 50 Hz (b) 2000 Hz when J_1 was illuminated (c) 50 Hz (d) 2000 Hz when J_2 was illuminated.

mW illumination power. The time of rise was found to be always shorter than the time of decay for J_1 and vice-versa for J_2 . Transit time, diffusion time and RC (R is a combination of the series resistance of PD and load resistance, and C is a combination of internal capacitance and load capacitance) time constant are the parameters which essentially control device operation speed in an ideal system. Furthermore, the contributions due to carrier trapping and de-trapping are added up in the presence of impurities. The presence of high defect densities has a significant effect on the value of τ_r and τ_d [22]. The speed of temporal operation of the PD becomes slower if the photogenerated carriers spend more time in the traps.

6.3.4.4. Effect of external bias on the speed of the photodetectors

In order to closely inspect the roles of the traps in carrier lifetimes, semi-logarithmic plots of photocurrent in the time domain on different biasing conditions were investigated which are shown in Figures. 6.12(a), (b), (c) and (d). Between these two SJs, only J_1 showed two decay

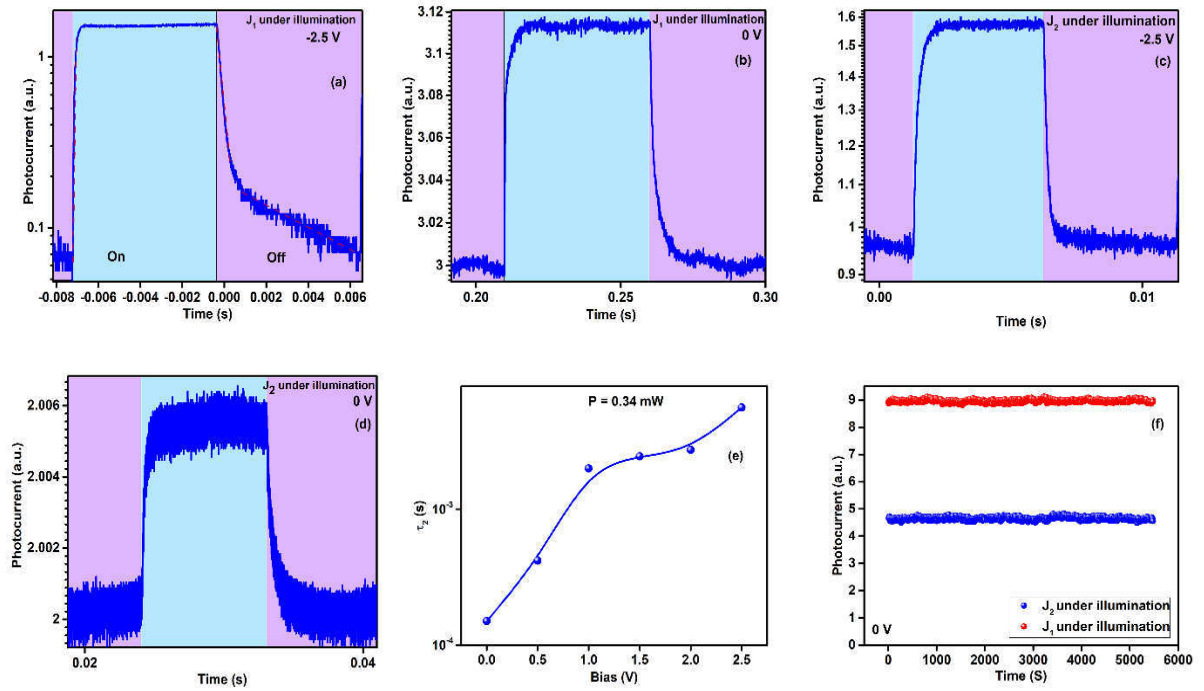


Figure 6.12. Enlarged view of temporal response in semi-log scale at a particular illumination wavelength and frequency of function generator (a) J_1 operating at 2.5 V (b) J_1 operating at 0 V (c) J_2 operating at 2.5 V (d) J_2 operating at 0 V. The color contrast differentiates the 'on' and 'off' states respectively. (e) Variation of the time constant of the 2nd decay channel of J_1 with increasing applied bias. (f) Stability of the devices at a fixed illumination wavelength and fixed bias (red sphere for J_1 and blue sphere for J_2).

channels during the time of recovery, at -2.5 V. After turning off the light, the value of the photocurrent rapidly decreased to 24% of its peak value by a fast process, thereafter the slow

decay process continued. Surprisingly, this behavior disappeared when J_1 was operated at 0 V bias where only a fast decay process existed which offered extra flexibility to tune its recovery speed by one order of magnitude. The decay curves (at different biases), thus obtained, were fitted by a bi-exponential decay function (given below) to extract the values of

$$I = I_L \left(A \exp \left(-\frac{t}{\tau_{d1}} \right) + B \exp \left(-\frac{t}{\tau_{d2}} \right) \right) \quad (6.1)$$

two decay constants accurately. Figure. 6.12(e) represents the dependence of τ_{d2} with variable applied bias. In this figure, the variation of τ_{d1} with applied bias is not included since it did not show anomalous bias dependent behavior like that of τ_{d2} . The value of (τ_{d2}/τ_{d1}) was found to be 23.4 at -2.5 V and became close to 1 at 0 V. The value of τ_d of J_1 at 0 V was 270 μ s. Monroy et al. have already studied the dependence of load resistance (R_L) on the response and recovery speed of the $\text{Al}_x\text{Ga}_{1-x}\text{N}$ system [34]. They have shown that the time constants (τ_r and τ_d) increase with an increase in the value of R_L . Here we have used the exact same value of R_L to measure the time constants for both the SJs. Although J_2 did not replicate the bias dependent behavior of J_1 , thus the effect of R_L can be easily eliminated. The origin of this behaviour will be discussed in detail in the explanation section of this chapter. The junctions J_1 and J_2 showed highly stable photodetection and no noticeable degradation in the value of photocurrents was observed even after illuminating the junctions over an hour (Figure. 6.12(f)).

6.3.4.5. Effect of illumination intensity on the speed of the photodetectors

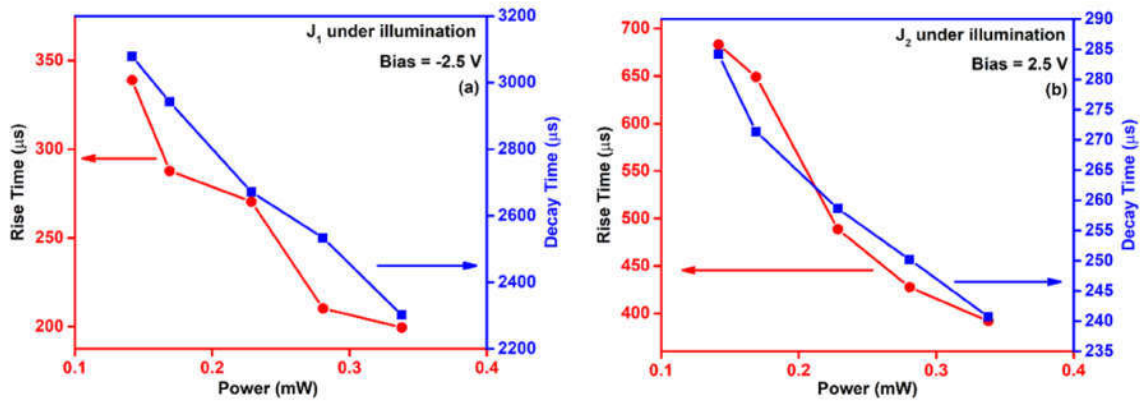


Figure 6.13. Bias dependent rise and decay time of (a) J_1 and (b) J_2 . The red line with filled square and blue line with a filled circle represents the rise and decay time respectively for the respective junctions.

We have also examined the behavior of time constants (τ_r , and τ_d) with different illumination power at a fixed reverse bias of 2.5 V. Figures. 6.13(a) and (b) show these variations for J_1 and

J_2 , respectively. The values of τ_r and τ_d were decreased with increasing illumination power which indicated that at high power, the PDs were able to detect a moderately high-frequency signal. At higher illumination power, the electric field intensity at the junction decreased due to a large amount of splitting of quasi-Fermi levels and subsequent reduction in the band bending. Hence, it is expected that the PD becomes slower with increasing illumination power. However, our observation is completely different which will be explained in section 6.3.6. It also signifies that the value of f_{3B} bandwidth was maximum when the device was illuminated by a high-power light source.

6.3.4.6. Broadband application

The photodetection capability of the PDs with different illumination wavelength was carried out to find out the region of their operation. These data are shown in Figures. 6.14(a), (b), (c), (d), (e) and (f). It was clearly indicated from the data that both the PDs were able to detect photons from ultraviolet to the near-infrared regime of the optical spectrum. Hence, these devices (Mg/ZnSnP_2 & Sn/ZnSnP_2) can act as a broadband PD.

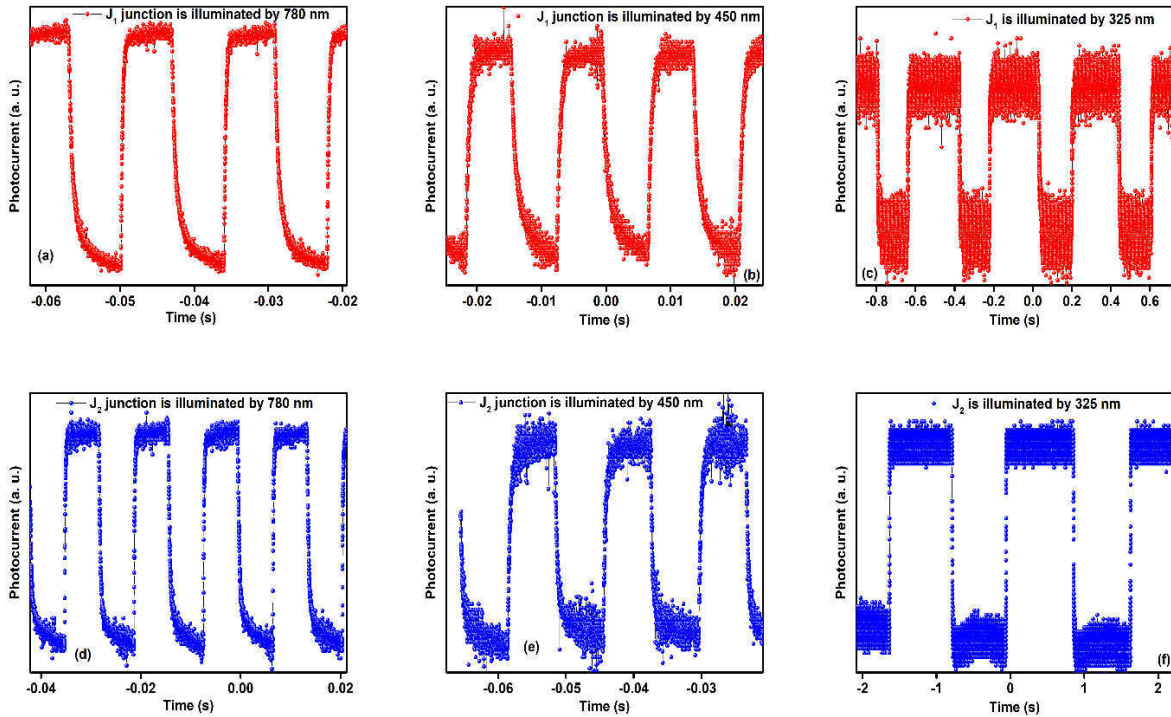


Figure 6.14. Photo-response of the PDs under different illumination wavelength (a) 780 nm for J_1 (b) 450 nm for J_1 (c) 325 nm for J_1 (d) 780 nm for J_2 (e) 450 nm for J_2 and (f) J_2 by 325 nm.

6.3.4.7. f_{3B} bandwidth of the photodetectors

The definition of the f_{3B} bandwidth of a PD is written in section 2.5.8 of chapter 2. Following that relation (equation 2.12), the obtained values of f_{3B} bandwidth were 1.75 kHz and 900 Hz for J_1 and J_2 , respectively.

6.3.5. Capacitance-frequency measurement

To estimate quantitatively the existing defects in the material, capacitance-frequency (C-f) measurements were carried out employing different biases under the dark condition and the results are shown in Figure. 6.15 (a). The value of C decreased (from 340 pF to 175 pF) with increasing frequency from 10^3 Hz to 10^6 Hz for a particular bias of 0.5 V. The nature of the C-f curve is correlated to the existing defects within the depletion region. Usually, the lifetimes associated with the deep level traps lying in between few milliseconds to few microseconds.

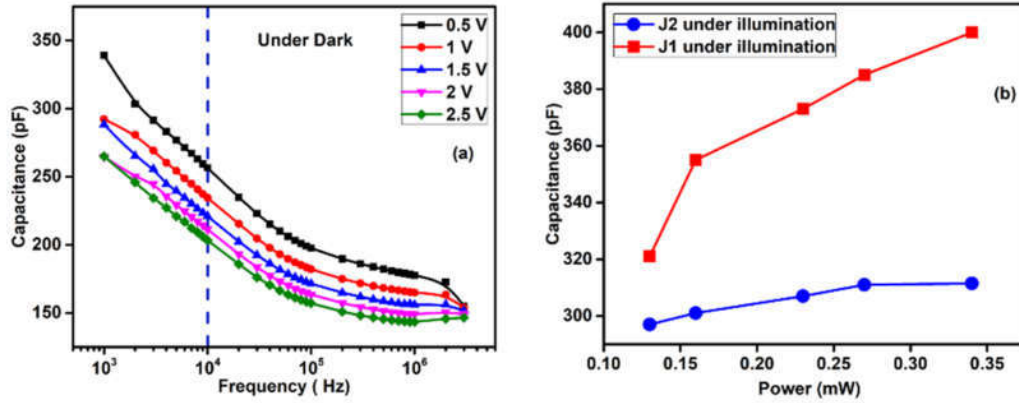


Figure 6.15. The variation of capacitance of the back-to-back connected Schottky junction (a) with frequency under different bias in dark. The dotted line in the figure is used to mark the change of capacitance with bias at a fixed frequency of 10 kHz. (b) under different illumination power. The red line with filled square and blue lines with filled circle in figure (b) represent for J_1 and J_2 junctions under illumination, respectively.

So, at a relatively low frequency, the charging and discharging of the traps can follow the alternating signal (which is superimposed with a DC signal) but it does not occur at higher frequencies. Hence, it was concluded that the extra contribution from the trap levels made the value of the capacitance higher at a lower frequency. Furthermore, the variation of capacitance with illumination intensity was measured and shown in Figure. 6.15(b). At a fixed frequency with increasing bias the value of C decreased which is in conformity to the p-type conductivity of the ZnSnP_2 thin film [21, 35]. The value of C increased with the increasing power of incident illumination and the increment at the junction J_1 was much stronger compared to the junction J_2 . The area-normalized capacitance for SJ is expressed in the following form [36]

$$C = \sqrt{\frac{q\epsilon_s N}{2(V_{bi}-V-\frac{kT}{q})}} = \frac{A}{W} \quad (6.2)$$

where ϵ_s is the permittivity of ZnSnP₂, N is space charge density, V_{bi} is the built-in potential, V is the applied bias, A is junction area and W is the width of the depletion region. Therefore, if the concentration of N is increased keeping all other parameters fixed, the value of C will rise. The width of the depletion region is modified by the capture of the photogenerated carriers at the impurity centers. After illumination, some of the photogenerated holes are being captured by the existing traps at the space charge region. Consequently, the carrier's density at the space charge region increases significantly which further explains the observed behavior in Figure. 6.15(b).

6.3.6. Explanations

Different types of impurities and defects generate multiple energy states in the forbidden energy gap in a semiconductor. These states are usually classified in two categories viz., (i) the recombination center having a higher probability of recombination of the captured carriers with opposite type as compared to the re-excitation of the carriers to the free state and (ii) the trapping center associated with the higher probability of thermal re-excitation of the captured

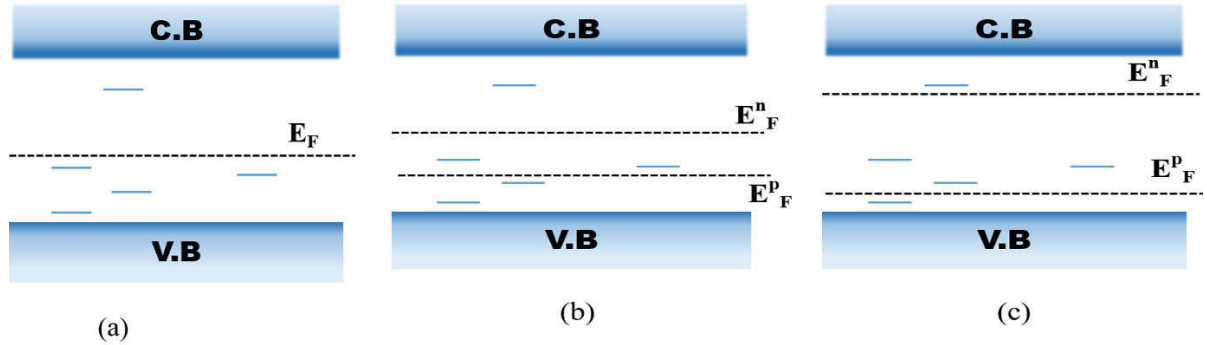


Figure 6.16. Model to explain super-linearity of photocurrent under different conditions (a) without illumination (b) under low power of illumination (c) under high illumination power. Here the dotted line designated as E_F , E_F^n , and E_F^p represents the position of Fermi level in dark, electron Fermi level with illumination and hole Fermi level with illumination, respectively. The blue lines depicted the energy states within the forbidden gap. The splitting of the quasi-Fermi level increases with increasing illumination intensity. The number of defect states between the electron and hole Fermi level increases with increasing illumination power.

carriers to the free state compared to recombination with their opposite counterpart. Usually, all the states are situated in between the hole and electron demarcation level are called the

recombination centers [37]. The position where a photogenerated carrier shares a fifty percent probability of thermal re-excitation from captured to the free-state is defined as the demarcation levels of respective carriers. These are eventually connected to the position of the Fermi level and hole capture cross-section of that particular state. Typically, the carriers have a higher lifetime in the recombination center than in the trapping center. In ZnSnP_2 the vacancy of Zn on Sn site (V_{Zn}) and that of Sn on Zn site (V_{Sn}) create different energy states in between the conduction band minima and the valance band maxima [21]. To illuminate the PDs, we have used a laser of energy (1.90 eV) which is higher than the bandgap (1.46 eV) of ZnSnP_2 film. The electron-hole pairs are produced inside the semiconductor under illumination and separated by the existing electric field at the depletion region. Before separation, some of the generated holes are captured by the recombination centers as well as the traps. While the holes

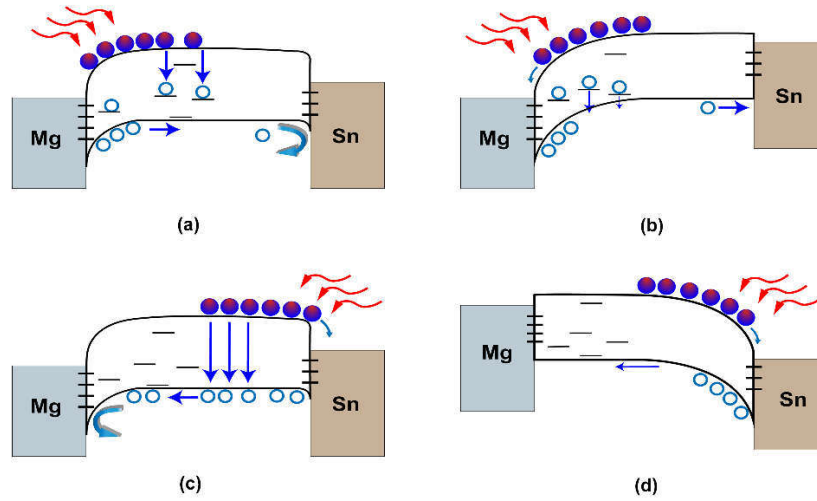


Figure 6.17. Energy band diagram (a) J_1 under illumination at 0 V (b) J_1 under illumination at 2.5 V (c) J_2 under illumination at 0 V (d) J_2 under illumination 2.5 V. The solid and hollow spheres represent electrons and hole respectively. The black lines at the junctions are the interface states and that of in between the two junctions are the defect states within the semiconductor. The hollow spheres within the bandgap illustrate the captured holes by the recombination centers/traps. The curved red arrows depict the incident illumination.

captured by the traps are released to the valence band, those captured by the recombination centers reside there. This process further increases the lifetime of the electrons in the conduction band which in turn helps the electrons to traverse the circuit multiple times before being recombined at the recombination centers with holes. This process is responsible for the gain of the PDs greater than unity. At equilibrium, electron, and hole Fermi levels coincide with each other, however, under illumination quasi splitting of those levels occurs which is schematically represented in Figures. 6.16(a), (b) & (c). When the power of the illumination is

increased, the quasi-Fermi level corresponding to the hole moves further towards the valance band maxima. Hence, the demarcation level also follows the same trend. Therefore, some of the hole trapping centers have converted to the recombination centers which further increase the number of electrons in the conduction band traveling multiple times in the circuit. Furthermore, this process also reduces the number of holes re-emitted from the trapping centers. The super-linear dependence of photocurrent and enhancement of device operation speed with increasing illumination power are effectively controlled by the process outlined above. A schematic representation of the energy band diagram of the fabricated PDs under self-powered and biased mode is shown in Figures. 6.17(a), (b), (c) & (d). To describe the non-identical voltage-dependent nature of both the junctions J_1 and J_2 , we have made a simple assumption that the traps within ZnSnP_2 thin films are not uniformly distributed. Moreover, we have also considered that the density of hole trapping centers is dominated over electron trapping centers which are highly populated near J_1 . The slow decay channel (τ_{d2}) is directly connected to the collection of trapped holes into the external circuit after their re-emission. Under the self-powered condition, the width of the depletion region is very thin. So, the maximum number of carriers are generated beyond the depletion region (Figure. 6.17(a)). Even though the trapped holes gain enough amount of energy to become free, the probability of reaching the other end is almost negligible due to the existing barrier at the other junction. However, with the application of the bias, the number of the captured holes within the space charge region increases (Figures. 6.17(b) & (d)) consequently, the probability of reaching the holes at the other contact increases.

6.3.7. Performance comparison with other state-of-the-art photodetectors

Table-6.1 Comparison of the figure of merits with other PDs

Name of the Sample	Applied Bias in V	Time of rise (τ_r)	Time of decay (τ_d)	Responsivity in AW^{-1}	Detectivity in J	Reference
Multilayer	0.1	3.0 s	3.3 s	17.21	NA	[32]

Ta₂NiSe₅						
GeSe nanosheet	4	0.1 s	0.1 s	3.5	NA	[38]
CZTS	0.15	391ms	221 ms	13	NA	[39]
Na doped CZTS	0.15	1.02 ms	29.8ms	63	NA	[40]
WS₂/Si	5	670 μs	998 μs	5.7	NA	[40]
MoSe₂	2.0	NA	NA	0.32	3.54x10 ¹²	[41]
MoSe₂ – Cu₂S nanoheterstructure	2.0	NA	NA	0.41	2.72x10 ¹²	[41]
SnO₂ nanoparticle/ SiO₂/ p-Si heterojunction	1	100 ms	70 ms	0.355	2.66x10 ¹²	[42]
MoS₂-WS₂	0V	4 ms	4 ms	0.04	4.34x10 ¹³	[10]
Bi₂O₂Se nanosheets	NA	2.8 ms	6.8 ms	6.5	8.3x10 ¹¹	[11]
(PEA)₂SnI₄	5	630 ms	3600 ms	16	1.92x10 ¹¹	[19]
CH₃NH₃SnI₃	2	1500 ms	400 ms	0.47	8.80x10 ¹⁰	[20]
Mg/ZnSnP₂/Sn	1.6	47μs	725μs	0.029	9.42x10 ¹⁰	[28]
Mg/ ZnSnP₂	0	200 μs	270 μs	0.1	4.62x10 ¹²	In this work

Mg/ ZnSnP₂	2.5	200 μ s	2300 μ s	4.7	1.19×10^{12}	In this work
Sn/ ZnSnP₂	0	400 μ s	240 μ s	0.03	10^{11}	In this work
Sn/ ZnSnP₂	2.5	390 μ s	240 μ s	12.7	4.78×10^{11}	In this work

A table of comparison of PD important figures of merits with the other state-of-the-art PDs is enlisted below. According to the values as enlisted in Table 1, the fabricated devices using ZnSnP₂, in the present work shows very high D value along with a fast temporal response. However, CZTS and Na doped CZTS have delivered better R than our device, in the case of response and recovery speed, they are lowered by three orders of magnitude. On the other hand, the PD synthesized using MoSe₂ and MoSe₂-Cu₂S deliver almost comparable D values whereas their R values are found to be poor even at relatively high bias. MoS₂-WS₂ PDs have exhibited the highest D value which is one order of magnitude higher than our fabricated devices. However, the values of the other determining parameters are nearly three orders of magnitude lower than the PDs are reported here. It may be noted that the performance of the fabricated device is better than the organic PDs from many aspects.

6.4. Conclusion

In this work, we have demonstrated a successful fabrication of a simple asymmetrical coplanar Mg/ZnSnP₂/Sn high-performance photodetector on a p-type Si by employing a less complicated and inexpensive growth process. The devices were characterized by variable illumination power and applied bias. Here, the two Schottky junctions J₁ and J₂ of the device were treated independently. In the self-powered configuration, the value of the responsivity and detectivity were 0.2 AW⁻¹ and 4.62×10^{12} Jones for the J₁ and 0.03 AW⁻¹ and 1.62×10^{11} Jones for the J₂ junction, respectively. During the biased mode of operation, these values become 4.7 AW⁻¹ and 1.19×10^{12} Jones in case of J₁ and 12.7 AW⁻¹ and 4.78×10^{11} Jones for J₂, respectively. For both the junctions, the power-dependent photocurrent showed a superlinear increment due to the conversion of traps into the recombination center. The response and recovery speed of the PDs were also studied under variable bias and illumination power. Under

an incident power of 0.34 mW, the rise and decay times for J_1 and J_2 were 200 μ s, 2300 μ s, and 390 μ s, 240 μ s, respectively at 2.5 V. In addition to the above observation, J_1 showed an unusual bias dependent decay channel which vanishes at 0 V. The appearance of an extra decay channel with bias is connected to trapping and de-trapping of carriers. The presence of defect states and capture of the photogenerated carriers by those states were confirmed from frequency and illumination dependent capacitance measurements. In the future work, it might be possible for the fabrication of multilayers ZnSnP_2 structure of variable bandgap by introducing disorder while keeping its lattice constant unaltered for photodetector application.

References

- [1] M. Izzetoglu, S. C. Bunce, K. Izzetoglu, B. Onaral and K. Pourrezaei, *IEEE Eng. Med. Biol. Mag.* (2007), 25, 54.
- [2] R. P. Chang and D. C. Perng, *Appl. Phys. Lett.* (2011), 99, 081103.
- [3] Y. Han, G. Wu, H. Li, M. Wang and H. Chen, *Nanotechnology*. (2010), 21, 1.
- [4] J. Sun, F. J. Liu, H. Q. Huang, J. W. Zhao, Z. F. Hu, X. Q. Zhang and Y. S. Wang, *Appl. Surf. Sci.* (2010), 257, 921.
- [5] X. Gong, M. Tong, Y. Xia, W. Cai, J. S. Moon, Y. Cao, G. Yu, C.-L. Shieh, B. Nilsson and A. J. Heeger, *Science*. (2009), 325, 1665.
- [6] G. Konstantatos and E. H. Sargent, *Nat. Nanotechnol.* (2010), 5, 391.
- [7] S. C. Dhanabalan, J. S. Ponraj, Q. Bao and H. Zhang, *Nanoscale*. (2016), 8, 6410.
- [8] Z. Huang, W. Han, H. Tang, L. Ren, D. S. Chander, X. Qi and H. Zhang, *2D Mater.* (2015), 2, 035011, 1.
- [9] J. D. Yao, Z. Q. Zheng, J. M. Shao and G. W. Yang, *Nanoscale*. (2015), 7, 14974.
- [10] J. D. Yao, Z. Q. Zheng and G. W. Yang, *J. Mater. Chem. C*. (2016), 4, 7831.
- [11] W. Wu, Q. Zhang, X. Zhou, L. Li, J. Su, F. Wang and T. Zhai, *Nano Energy*. (2018), 51, 45.
- [12] J. Li, Z. Wang, Y. Wen, J. Chu, L. Yin, R. Cheng, L. Lei, P. He, C. Jiang, L. Feng and J. He, *Adv. Funct. Mater.* (2018), 28, 1706437.
- [13] H. M. Hill, A. F. Rigosi, K. T. Rim, G. W. Flynn and T. F. Heinz, *Nano Letters*. (2016), 16, 4831.
- [14] K. F. Mak, C. Lee, J. Hone, J. Shan and T. F. Heinz, *Phys. Rev. Lett.* (2010), 105, 2, 136805.
- [15] T. Low and P. Avouris, *ACS Nano*. (2014), 8, 1086.
- [16] F. Xia, T. Mueller, R. Golizadeh-Mojarad, M. Freitag, M. Y. Lin, J. Tsang, V. Perebeinos, and P. Avouris, *Nano Lett.* (2009), 9, 1039.

- [17] L. Wang, I. Meric, P. Y. Huang, Q. Gao, Y. Gao, H. Tran, T. Taniguchi, K. Watanabe, L. M. Campos, D. A. Muller, J. Guo, P. Kim, J. Hone, K. L. Shepard and C. R. Dean, *Science*. (2013), 342, 614.
- [18] R. Dong, Y. Fang, J. Chae, J. Dai, Z. Xiao, Q. Dong, Y. Yuan, A. Centrone, X. C. Zeng, and J. Huang, *Adv. Mater.* (2015), 27, 1912.
- [19] L. Qian, Y. Sun, M. Wu, C. Li, D. Xie, L. Ding and G. Shi, *Nanoscale*. (2018), 10, 6837.
- [20] A. Waleed, M. M. Tavakoli, L. Gu, Z. Wang, D. Zhang, A. Manikandan, Q. Zhang, R. Zhang, Y. Chueh and Z. Fan, *Nano Lett.* (2017), 17, 523.
- [21] S. Mukherjee, T. Maitra, A. Nayak, S. Mukherjee, A. Pradhan, M. K. Mukhopadhyay, B. Satpati and S. Bhunia, *Mat. Chem. Phys.* (2018), 204, 147.
- [22] S. Mukherjee, T. Maitra, A. Pradhan, S. Mukherjee, G. Manna, S. Bhunia and A. Nayak, *Sol. Energy Mater Sol. Cells*. (2019), 189, 181.
- [23] M. Zheng, P. Gui, X. Wang, G. Zhang, J. Wan, H. Zhang, G. Fang, H. Wu, Q. Lin and C. Liu, *Appl. Surf. Sci.* (2019), 481, 437.
- [24] A. D. Martinez, A. N. Fioretti, E. S. Toberer and A. C. Tamboli, *J. Mater. Chem. A*. (2017), 23 11418.
- [25] J. Gao, J. M. Luther, O. E. Semonin, R. J. Ellingson, A. J. Nozik and M. C. Beard, *Nano Lett.* (2011), 11, 1002.
- [26] A. Niemegeers and M. Burgelman, *J. Appl. Phys.* (1997), 81, 2881.
- [27] H. Tanaka, T. Kawazoe and M. Ohtsu, *App. Phys. B*. (2012), 108, 51.
- [28] R. Dong, Y. Fang, J. Chae, J. Dai, Z. Xiao, Q. Dong and Y. Yuan, *Adv. Mater.* (2015), 27, 1912.
- [29] Md S. Mahdi, K. Ibrahim, A. Hmood, N. M. Ahmed, S. A. Azzez and F. I. Mustafa, *RSC Adv.* (2016), 6, 114980.
- [30] K. W. Liu, J. G. Ma, J. Y. Zhang, Y. M. Lu, D. Y. Jiang, B. H. Li, D. X. Zhao, Z. Z. Zhang, B. Yao and D. Z. Shen, *Solid State Electron.* (2007), 51, 757.
- [31] Z. Zheng, L. Gan, H. Li, Y. Ma, Y. Bando, D. Golberg and T. Zhai, *Adv. Funct. Mater.* (2015), 25, 5885.

- [32] L. Li, W. Wang, L. Gan, N. Zhou, X. Zhu, Q. Zhang, H. Li, M. Tian and T. Zhai, *Adv. Funct. Mater.* (2016), 26, 8281.
- [33] V. Klee, E. Preciado, D. Barroso, A. E. Nguyen, C. Lee, K. J. Erickson, M. Triplett, B. Davis, I. Lu, S. Bobek, J. McKinley, J. P. Martinez, J. Mann, A. A. Talin, L. Bartels and F. Léonard, *Nano Lett.* (2015), 15, 2612.
- [34] E. Monroy, F. Calle, J. L. Pau, F. J. Sanchez and E. Munoz, *J. App. Phys.* (2000), 88, 2081.
- [35] A. A. Abdurakhimov, V. L. Kradinova, A. Z. Parimbekov and V. Y. Rud, *Sov. Phys. Semicond.* (1982), 16, 156.
- [36] S. M. Sze, K. K. Ng, *Physics of Semiconductor Devices*, Wiley-Interscience, New Jersey, 2007.
- [37] A. Rose, *Concepts in Photoconductivity and Allied Problems*, Wiley-Interscience, New York, 1963.
- [38] B. Mukherjee, Y. Cai, H. R. Tan, Y. P. Feng, E. S. Tok and C. H. Sow, *ACS Appl. Mater. Interfaces.* (2013), 5, 9594.
- [39] O. P. Singh, A. Sharma, K. S. Gour, S. Husale and V. N. Singh, *Sol. Energy Mater Sol. Cells.* (2016), 157, 28.
- [40] C. Lan, C. Li, S. Wang, T. He, T. Jiao, D. Wei, W. Jing, L. Li and Y. Liu, *ACS Appl. Mater. Interfaces.* (2016), 8, 18375.
- [41] Md. S. Hassan, S. Bera, D. Gupta, S. K. Ray and S. Sapra, *ACS Appl. Mater. Interfaces.* (2019), 11, 4074.
- [42] C. Ling, T. Guoa, W. Lua, Y. Xionga, L. Zhua and Q. Xue, *Nanoscale.* (2017), 9, 8848.